Electronic Supplementary Material (ESI) for Journal of Materials Chemistry A.

Supporting Information

Coupling Homogeneous and Heterogeneous Catalysis for the Efficient and Selective Activation of H_2O_2

JiaWei Yan,[a,c] Siyuan Wei,[a,c] Yalan Lin,[a,c] Yanfei Zhu,[b] Zhiwu Zhong,[a,c] Yanting Zheng,[a,c] Zanyong Zhuang[a,c] and Yan Yu*[a,c]*

[a]College of Materials Science and Engineering, Fuzhou University, New Campus, Minhou, Fujian 350108, China

[b]Tsinghua-Berkeley Shenzhen Institute & Tsinghua Shenzhen International Graduate School Shenzhen, 518055, P. R. China

[c]Key Laboratory of Advanced Materials Technologies, Fuzhou University, Fuzhou 350108, China

E-mail: zyzhuang@fzu.edu.cn, yuyan@fzu.edu.cn

EXPERIMENTAL SECTION

Characterization. The crystal structures of samples were determined with a Panalytical X'pert MPD X-ray diffractometer (XRD). The Fourier transform infrared (FTIR) spectra of all the catalysts were recorded by using a TJ270-30A infrared spectrophotometer (Tianjin, China). The morphology of the samples was examined with a field emission scanning electron microscope (SEM, Philips XL30). UV−vis diffuse reflection spectroscopy (DRS) was performed on a Hitachi UV-3010 UV−vis spectrophotometer. X-ray photoelectron spectrometry (XPS, PHI 5000 Versa Probe) was applied to the surface analysis of the samples. The photoluminescence (PL) spectra and the time-resolved fluorescence decay spectra of the photocatalysts were measured on the Varian Cary Eclipse spectrometer with an excitation wavelength of 325 nm. EPR spectra were recorded at room temperature by using a Bruker EMXnano spectrometer. BET specific surface areas were calculated using the Brunauer-Emmett-Teller (BET) equation in the relative pressure range (P/P_0) 0−1. The intermediate products were identified using a liquid chromatography–quadrupole time-of-flight tandem mass spectrometry (LC-QTOF-MS, G6520B).

Degradation experiments. The catalytic activity of the ternary systems was performed by the degradation of ENR, using a Xe lamp (500 W) equipped with a UV cut off filter (λ> 420 nm) as the irradiation source. There was no need to adjust the pH of the solution during the test. Reactions were triggered by adding appropriate dosages of $FeSO_4$, catalysts and H_2O_2 simultaneously into the reaction solution containing ENR (50mL). Then 1.5 mL reaction solution were filtrated through 0.22 μm nylon membrane. An HPLC chromatograph equipped with a UV–vis detector set at 270 nm was used to determine the concentration of ENR. A mixture of 0.1% formic acid and acetonitrile (70/30, v/v) at a flow rate of 0.8 mL/min was used as the mobile phase. After 60 min reactions, the residual catalyst powders for reuse were collected.

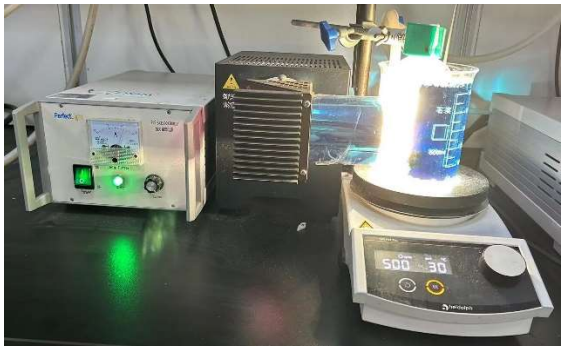

The experimental set-up for photocatalytic degradation.

Antimicrobial experiments. The antimicrobial ability of the Mn-C_3N_4 ternary system was investigated against Escherichia coli (E. coli; commercially available strains). Model bacterium strains (200 μL) were added to a tube with sterile Luria-Bertani (LB) broth (10 mL). The bacteria were cultured in an incubator shaker at 37 °C, 200 rpm for 8 h. For disinfection test, appropriate dosages of $FeSO_4$, catalysts and H_2O_2 were put into 50 ml deionized water, followed by adding a certain amount of prepared bacterial solution (containing cultured E. coli was 50 ml of 10^8 colony-forming units (CFU) mL^{-1}), using a Xe lamp (500 W) equipped with a UV cut off filter (λ> 420 nm) as the irradiation source, after being reacted at 30 °C, 100 rpm for 1 h. 0.5 mL suspension was pipetted out. The suspension was diluted with standard serial dilution. The diluted suspension (100 μL) was spread onto an agar medium. Bacterial colonies were counted after being cultivated at 37 °C for 12 h. Each system was tested three times.

Supplementary Information for Experimental Section

The measurement of consuming H_2O_2 during Mn-C_3N_4 ternary system

The H_2O_2 consumption during Mn-C_3N_4 ternary system is measured by a traditional cerium sulfate $Ce(SO_4)_2$

detection method based on the mechanism that a yellow solution of Ce^{4+} can be reduced by H_2O_2 to colorless Ce^{3+} (eq. S1). Thus, the concentration of Ce^{4+} before and after the reaction can be measured by the UV-vis spectroscopy. The absorption peak used for the measurement was 316 nm. The concentration of H_2O_2 can be determined by eq. S2. Briefly, the yellow transparent $Ce(SO_4)_2$ solution (1 mM) was prepared by dissolving 33.2 mg $Ce(SO_4)_2$ in 100 mL 0.5 M sulfuric acid solution. At specific time intervals, the 0.5 mL reaction solution filtrated through 0.22 μm membranes were collected in 5 mL centrifuge tube and then mixed with 2.5 mL $Ce(SO_4)_2$ solution (1 mM), and then shaken for 30 s. Finally, the obtained solutions were detected by UV-vis spectroscopy at 316 nm. To obtain the calibration curve, H_2O_2 with known concentration was added to $Ce(SO_4)_2$ solution and measured by a UV/vis spectrometer. Based on the linear relationship between the signal intensity and Ce^{4+} concentration, the H_2O_2 concentrations could be obtained.

$$2Ce^{4+} + H_2O_2 \rightarrow 2Ce^{3+} + 2H^+ + O_2 \quad \text{(S1)}$$

$$M = \frac{MCe^{4+}}{2} \quad \text{(S2)}$$

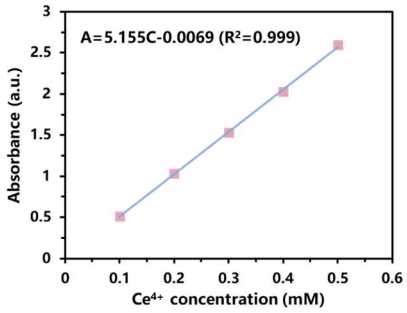

UV-vis spectroscopy calibration curve of Ce^{4+} solutions with different concentrations.

The change of Fe(II) concentrations during ternary systems

The change of Fe(II) concentrations during ternary systems was measured by 1,10-phenanthroline detection method. The Fe^{2+} combine with the 1,10-phenanthroline to form a reddish-orange colored complex that is measured by UV-vis spectroscopy at 510 nm. Briefly, the 5% 1,10-phenanthroline solution was prepared by dissolving 5 mg 1,10-phenanthroline in 95 mL deionized water. At specific time intervals, the 2.5 mL reaction solution were collected in 5 mL centrifuge tube and then mixed with 0.4 mL 1,10-phenanthroline solution (5%), and then shaken for 30 s. Finally, the obtained solutions were detected by UV-vis spectroscopy at 510 nm. To obtain the calibration curve, Fe^{2+} with known concentration was added to 1,10-phenanthroline solution and measured by a UV/vis spectrometer. Based on the linear relationship between the signal intensity and known Fe^{2+} concentration, the Fe^{2+} concentrations could be obtained.

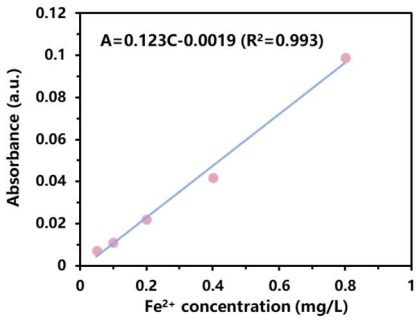

UV-vis spectroscopy calibration curve of Fe^{2+} solutions with different concentrations.

The quantification of •OH and $•O_2^-$ during ternary systems

Benzoic acid (BA) was used as a probe molecule to react with •OH from H_2O_2 activation. The 1.5 mL reaction solution filtrated through 0.22 μm membranes. HPLC was used to determine the p-hydroxybenzoic acid (p-HBA) concentration. The mobile phase was acetonitrile/water (50/50, v/v) and the detection wavelength was 270 nm. Injection volume, flow rate of mobile phase, and column temperature were fixed at 10 μL, 1.0 mL/min and 35 °C, respectively. Given that 5.87 ± 0.18 moles •OH reacting with BA produced one mole p-HBA. The cumulative •OH concentration is therefore approximately 5.87 times that of p-HBA concentration. Given the fact that 1 mol Nitroblue tetrazolium (NBT) can react with 4 mol $•O_2^-$. We quantified the concentration of generated $•O_2^-$ in the Fenton suspension by recording the residual concentration of NBT on a UV-vis spectrophotometer (maximum absorbance at 260 nm). The selectivity of activation H_2O_2 to $•O_2^-$ and activation H_2O_2 to •OH within 30 min, were calculated by the following eq. S3 and eq. S4, respectively.

$$\text{Selectivity (to •OH) (\%)} = \frac{[•\mathrm{OH}]_t}{[•\mathrm{OH}]_t+[•\mathrm{O_2^-}]_t} \times 100 \quad \text{(S3)}$$

$$\text{Selectivity (to } •O_2^-\text{) (\%)} = \frac{[•\mathrm{O_2^-}]_t}{[•\mathrm{OH}]_t+[•\mathrm{O_2^-}]_t} \times 100 \quad \text{(S4)}$$

Electrochemical measurement

Amperometric i−t curves and transient photocurrents were measured with an electrochemical analyzer (CHI660E, Shanghai Chenhua Co., China.). Experiments were carried out in 0.1M Na_2SO_4 solution, using the FTO glass containing catalysts (It was fabricated by dropping the suspension liquid (2 mg powders dispersed in 0.5 mL N,N-Dimethylformamide) on the FTO glass with a 0.25 cm^2 working area) as working electrode, the Ag/AgCl electrode as the reference electrode, and the Pt as the counter electrode. Cyclic voltammetry (CV) measurement was carried out on an electrochemical work station (CHI660E, Shanghai Chenhua Co., China) with three-electrode electrochemical cell equipped with glassy carbon electrode act as working electrode, with a Pt as a counter electrode and Ag/AgCl electrode act as reference electrode in $FeSO_4$, $FeSO_4$+g-C_3N_4, $FeSO_4$+Cu-C_3N_4, $FeSO_4$+Ni-C_3N_4 and $FeSO_4$+Mn-C_3N_4 solutions ([Fe^{2+}]=0.56 ppm, [sample]=0.1 g/L). A KCl (0.1 M) solution containing 5.0mM $K_3[Fe(CN)_6]/K_4[Fe(CN)_6]$ was used as the electrode solution for the electrochemical impedance spectroscopy (EIS) measurements (frequency: 1 Hz to 100 kHz) (PARSTAT MC). Mott-Schottky (M-S) plots (PARSTAT MC) were obtained by using 0.2 M Na_2SO_4 solution as the electrolyte, with the potential ranging from -1.2 V to 1.2 V (vs. Ag/AgCl) at frequencies of 0.5 kHz, 1.0 kHz and 1.5 kHz. The electrochemical studies were performed at room temperature of 25 °C.

In-Situ FT-IR measurement

The H_2O_2 evolution process over Mn-C_3N_4 and Fe^{2+} adsorbed Mn-C_3N_4 surface was conducted in a reaction chamber assembled in the FT-IR spectrometer (iS50, Thermo Scientific) equipped with a diamond internal reflection element and liquid-nitrogen cooled HgCdTe mercury cadmium telluride (MCT) detector. The spectrograms were collected from 650 to 4000 cm^{-1} at a resolution of 4 cm^{-1} (number of scans = 32). Prior to experiment, the 1 mg catalyst powders and 70 mg potassium bromide were placed in a sample crucible to grind. After grinding, and then pressed to form thin film, H_2O_2 were dropped on the thin film, which was followed by placed on the sample cup in the reaction chamber. In order to eliminate the air effect, Flowing the Ar gas through the reaction chamber to removed air. Before collected spectra, the thin film was subtracted as background. The spectra were finally collected at a certain time (5 min, 10 min, 15 min, 30 min). For the H_2O_2 evolution process over Fe^{2+} adsorbed Mn-C_3N_4, the measurement condition were same with those of Mn-C_3N_4, except for adding $FeSO_4$ solution on the thin film.

DFT calculation

We have employed the Vienna Ab initio Simulation Package (VASP) to perform all density functional theory (DFT) calculations within the generalized gradient approximation (GGA) using the Perdew-Burke-Ernzerhof (PBE) functional. We have chosen the projected augmented wave (PAW) potentials to describe the ionic cores and take valence electrons into account using a plane wave basis set with a kinetic energy cutoff of 450 eV. Geometry optimizations were performed with the force convergence smaller than 0.05 eV/Å. Monkhorst-Pack k-points of 2×1×1 was applied for all the calculations. Spin-polarization effect was also considered. The DFT-D3 empirical correction method was employed to describe van der Waals interactions.

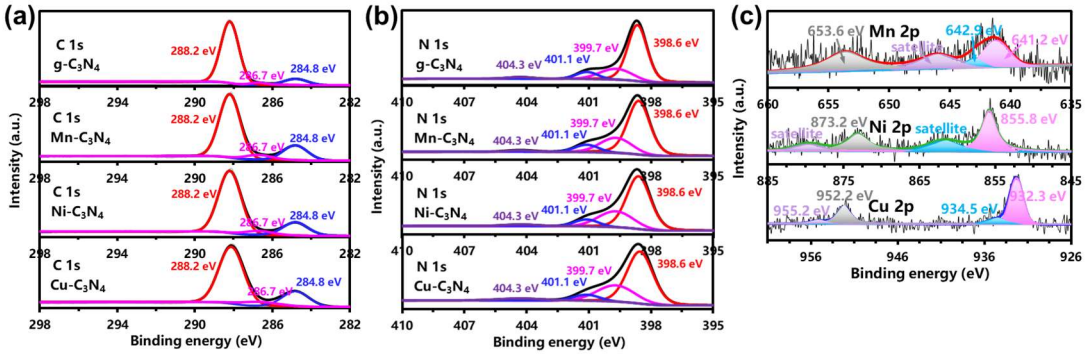

Fig. S1 (a) C1s, (b) N1s, (c) Mn 2p, Ni 2p, and Cu 2p XPS spectra of g-C_3N_4 and M-C_3N_4.

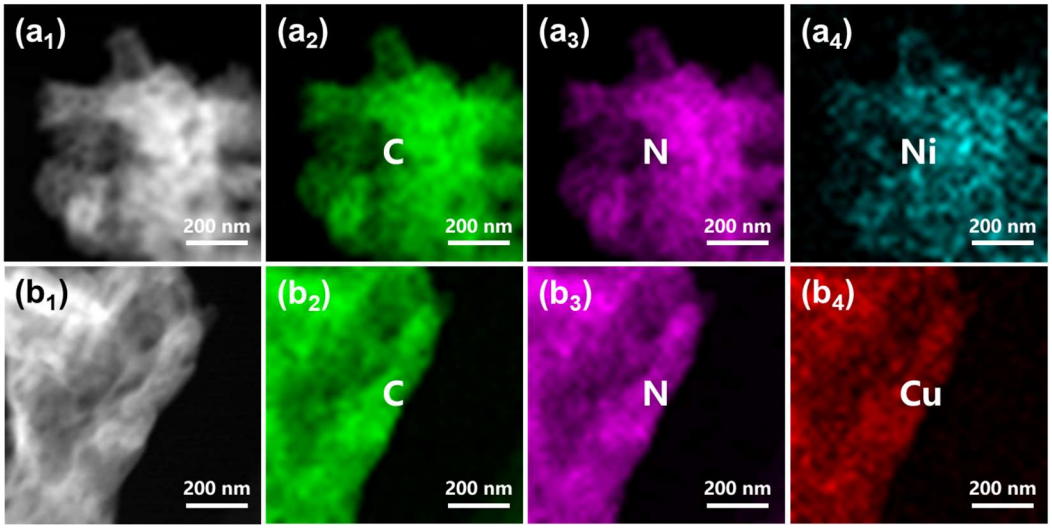

Fig. S2 HAADF images and the corresponding EDS elemental mappings of Ni-C_3N_4 (a_1-a_4) and Cu-C_3N_4 (b_1-b_4).

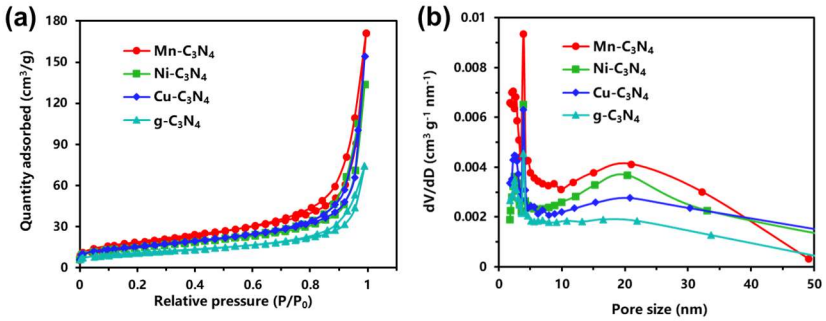

Fig. S3 (a) N_2 adsorption-desorption isotherms and (b) the corresponding pore size distribution curves of g-C_3N_4 and M-C_3N_4.

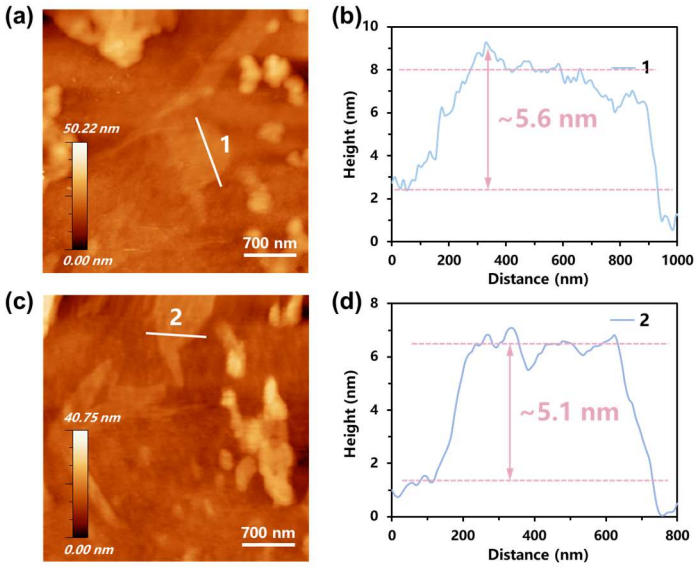

Fig. S4 AFM image and the corresponding height image of (a-b) g-C_3N_4 and (c-d) Mn-C_3N_4.

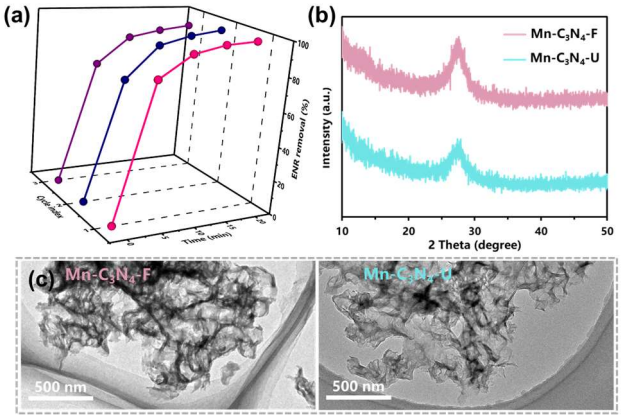

Fig. S5 a) Recyclability of Mn-C_3N_4 for ENR degradation in the Fe^{2+}/H_2O_2/Mn-C_3N_4 system, b) XRD patterns, c) SEM images of Mn-C_3N_4 before and after the catalytic reaction. The postfix 'F' indicates fresh sample, the 'U' indicates used catalyst after multi-cycle catalytic reaction.

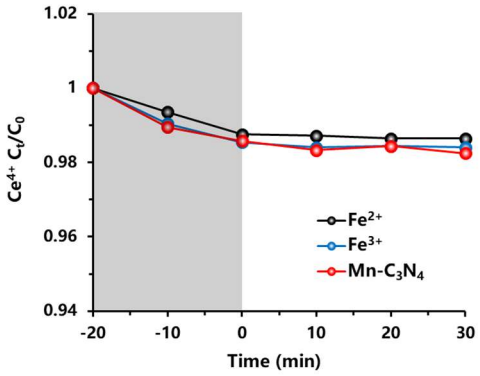

Fig. S6 Comparative experiments of H_2O_2 consumption.

Comparative experiments of H_2O_2 consumption. The Fe^{2+}, Fe^{3+} and Mn-C_3N_4 in the system will not affect the determination of concentration of Ce^{4+} measured by the UV-vis spectroscopy.

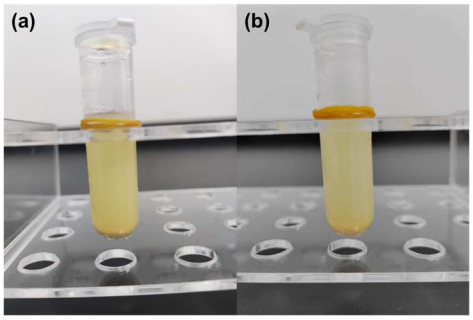

Fig. S7 The image of O_2 generation in the H_2O_2/Mn-C_3N_4 system (a) under dark and (b) light within 10 min.

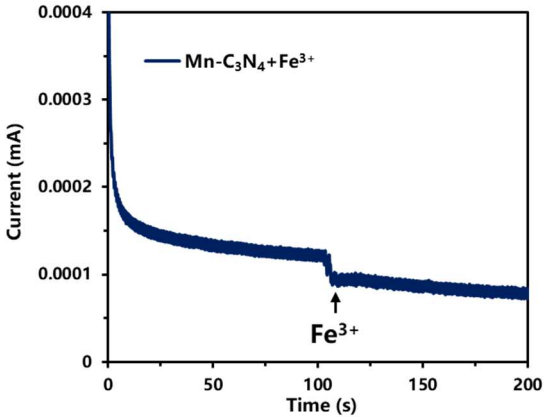

Fig. S8 Amperometric i–t curves of the FTO glass coated with Mn-C_3N_4 as the working electrode with visible light irradiation (Fe^{3+} = 4.6 μM, initial pH = 7.0±0.1, initial potential = +0.5 V).

Positioning the target of electron transfer pathway. We try to position the target of electron transfer pathway in the catalytic process with electrochemistry test. Amperometric i-t curves of "Mn-C_3N_4 and trace Fe^{3+}" system is tested, when Fe^{3+} is injected into the system, a negative current detected on the Mn-C_3N_4 electrode indicating that electron transferred from Mn-C_3N_4 to Fe^{3+}.

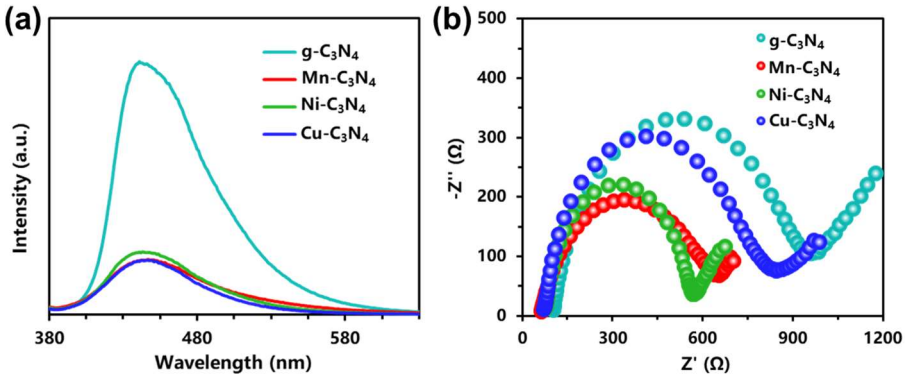

Fig. S9 (a) Room temperature PL spectra and (b) EIS Nyquist plots of g-C_3N_4 and M-C_3N_4.

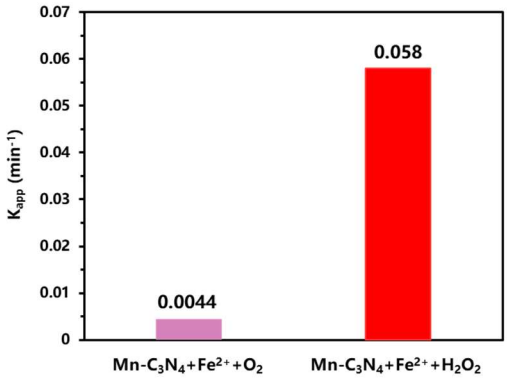

Fig. S10 The kinetic rate constants of $Fe^{2+}/O_2/Mn\text{-}C_3N_4$ system in ENR degradation.

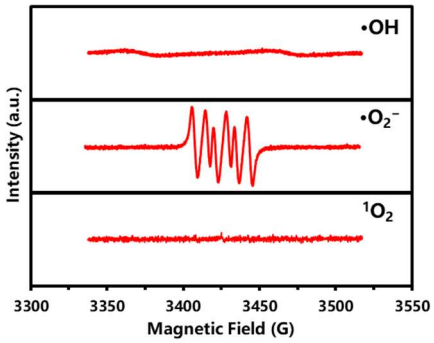

Fig. S11 DMPO-•OH EPR spectra, DMPO-$•O_2^-$ EPR spectra and TEMP-$^1O_2$ EPR spectra in $Fe^{2+}/H_2O_2/Mn\text{-}C_3N_4$ system under visible light ([DMPO] = 30 mM, [TEMP]= 60mM).

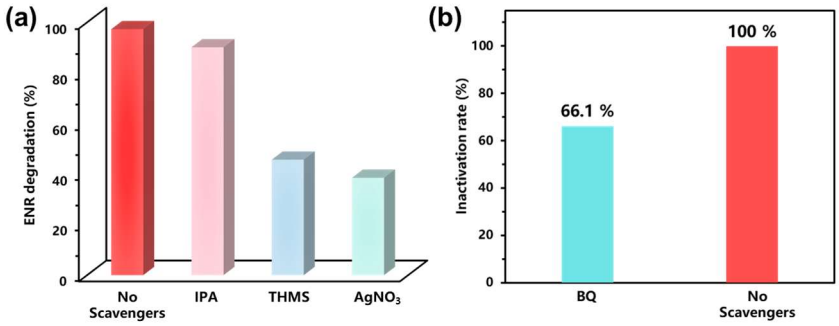

Fig. S12 (a) Effect on ENR degradation by $Fe^{2+}/H_2O_2/Mn\text{-}C_3N_4$ system under the presence of reactive radical scavengers including isopropanol (IPA, 25mM), trichloromethane (THMS, 250mM) and $AgNO_3$ (40mM). (b) Images of the inactivation of E. coli by $Fe^{2+}/H_2O_2/Mn\text{-}C_3N_4$ system in the presence of radical scavenger including p-benzoquinone (BQ, 0.2mM).

Verifying the major active free radicals in the disinfection experiment. Isopropanol (IPA),[1] trichloromethane (THMS),[2] and $AgNO_3$[3] as scavengers are added into the $Mn\text{-}C_3N_4$ system. Consistent with the EPR analysis, the oxidation activity of the $Mn\text{-}C_3N_4$ system does not decrease at all in the presence of IPA (quenching agent for •OH), while the oxidation activity is significantly inhibited after the introduction of THMS (quenching agent for $•O_2^-$) and $AgNO_3$ (quenching agent for e^-). Meanwhile, in $Mn\text{-}C_3N_4$ system, BQ (quenching agent for $•O_2^-$)[4] also show a certain inhibitory effect for the inactivation of E. coli.

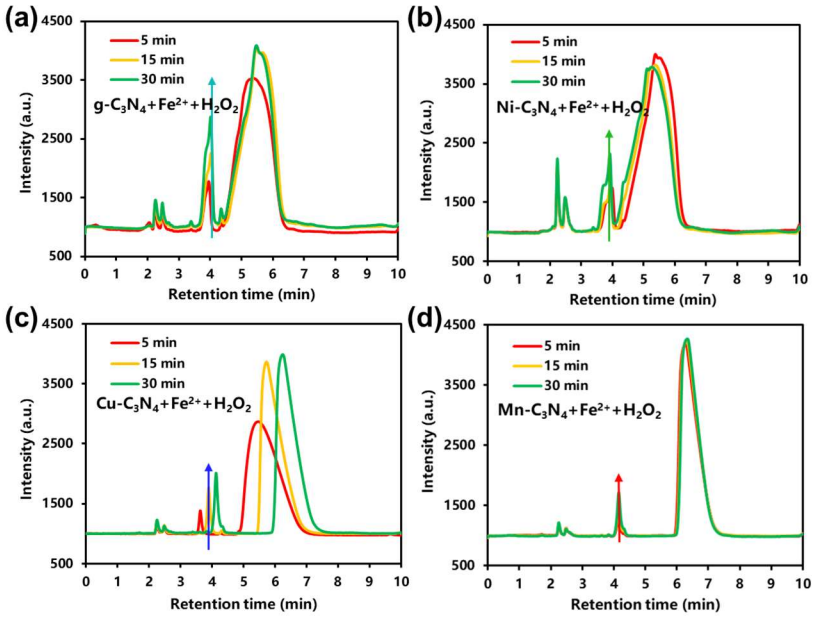

Fig. S13 (a-d) HPLC of p-Hydroxybenzoic acid (p-HBA) converted from Benzoic acid (BA) (0.5 mM) in different systems within 30 minutes under visible light.

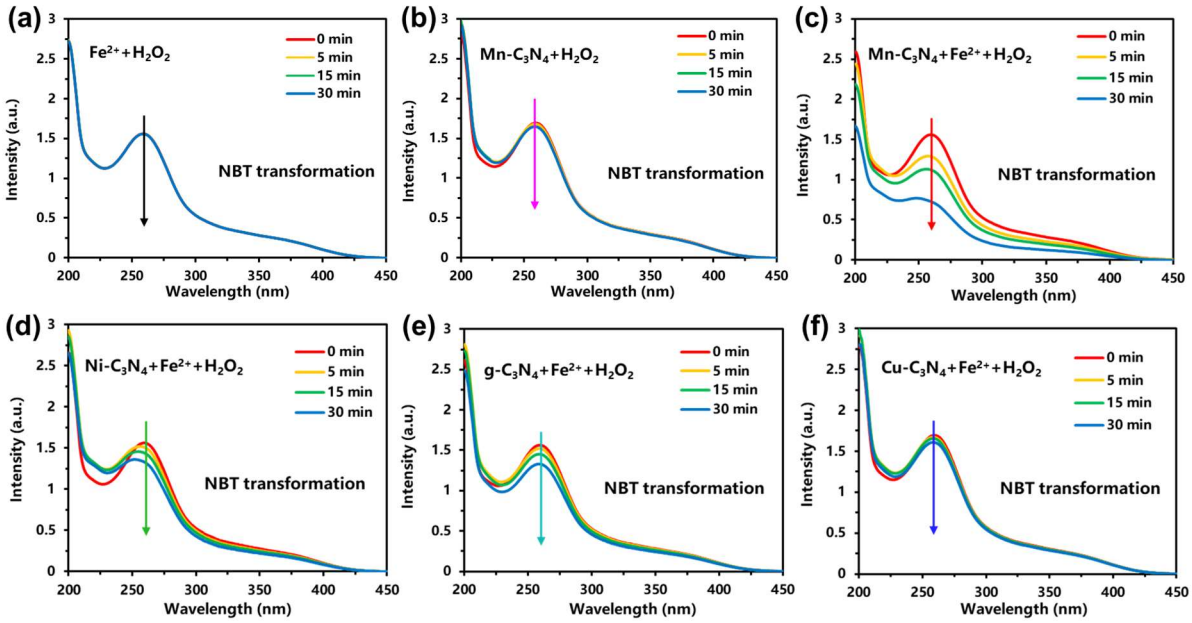

Fig. S14 UV vis spectra of Nitrotetrazolium Blue chloride (NBT) (0.025 mM) solution catalyzed by different systems (c-f) within 30 minutes under visible light.

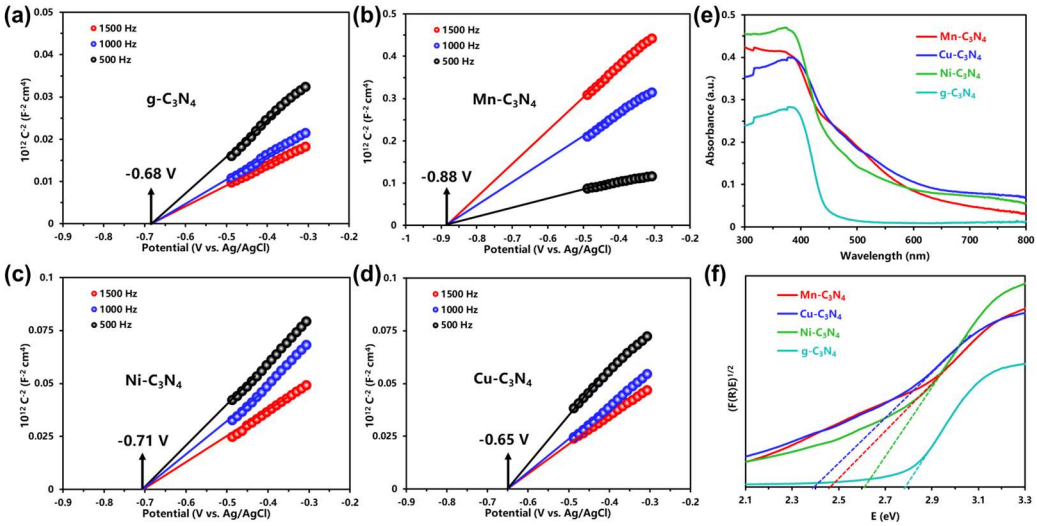

Fig. S15 (a-d) Mott–Schottky plots, (e) UV-vis-NIR diffuse reflectance spectra, and (f) the corresponding plot of $(\alpha hv)^2$ vs. photon energy (hy) of g-C_3N_4 and M-C_3N_4.

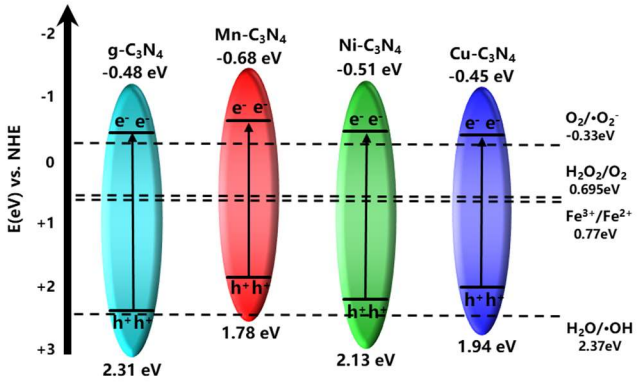

Fig. S16 Bandgap structures of g-C_3N_4 and M-C_3N_4.

Reaction potentials and the energy level diagrams. The band structure of Mn-C_3N_4 is thermodynamically suitable for Fe(III)/Fe(II) conversion under visible light. As shown in Figure 8, the photogenerated electrons in conduction band (CB) of Mn-C_3N_4 (-0.68 eV vs NHE) were negative enough to reduce the Fe(III) to Fe(II) (E_0= 0.77 V vs NHE). While the photogenerated holes in valence band (VB) of Mn-C_3N_4 (1.78 eV vs NHE) were positive enough to oxidize the H_2O_2 to O_2 (E_0= 0.695 V vs NHE).

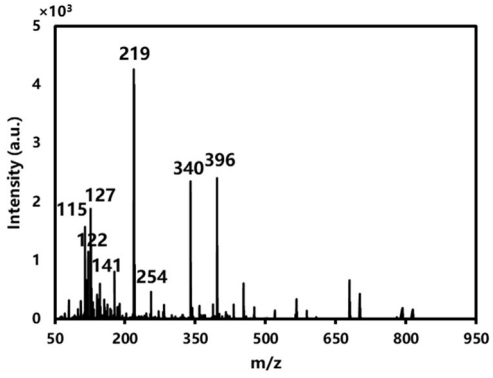

Fig. S17 Mass spectra of degradation intermediates of ENR (m/z = 360).

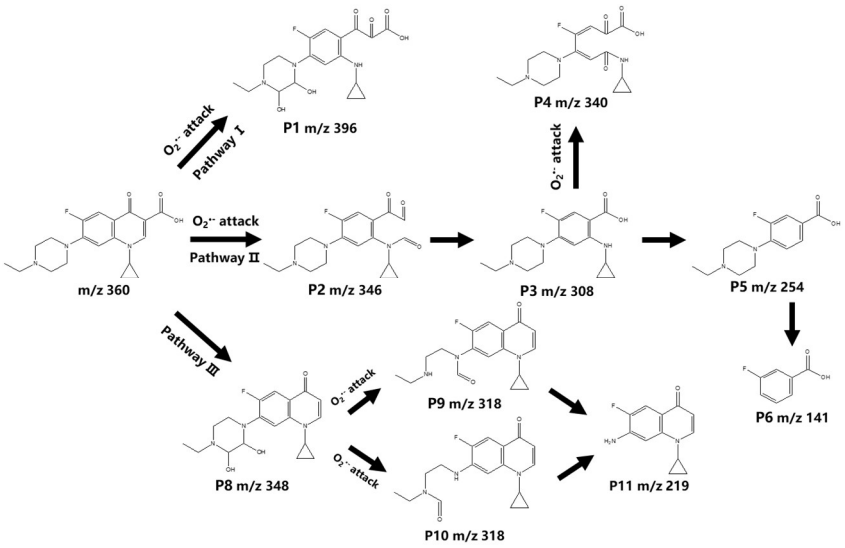

Fig. S18 Possible degradation pathways for ENR removal by $Fe^{2+}/H_2O_2/Mn\text{-}C_3N_4$ system.

Degradation pathways and intermediates identification. The intermediate products of ENR were detected by LC-QTOF-MS, and the possible degradation pathways of ENR are shown in Fig. 9. In pathway I, the quinolone of ENR was cracked and the alkyl group adjacent to N in the piperazine ring was oxidized and generated products 1. Pathway II mainly includes the open of quinolone moieties, benzene ring and the loss of the piperazinyl substituent. Due to the strong oxidizing capacity of the reactive groups, the quinolone and benzene rings would be destroyed in succession and generated products 2 - products 4 in turn. This pathway was similar to that in Wen's study.[5] Further, the N26 of products 3 was attacked to form the products 5. It could form simpler compound products 6 though removal of piperazinyl moieties. Pathway III was mainly the decarboxylation and the loss of the piperazine ring, which took place at the N1 and N4 positions on the piperazine ring. Product 8 was diol intermediate, which was formed owing to the oxidation of the alkyl group adjacent to N in the piperazine ring and decarboxylation.[6] The piperazine ring was further oxidized and opened by $\bullet O_2^-$ to generate products 9 or 10.[7-8] Products 11 were generated by the complete loss of the piperazinyl group from products 9 or 10.

Table S1. Results of EXAFS analyses.

Sample	Shell	N	R (Å)	σ^2 (10^{-3} Å)	ΔE_0 (eV)
$Mn\text{-}C_3N_4$	Mn-N	3.35	2.25	-0.93	10.09

Table S2. Comparison of pollutants degradation reactivity for synergistic H_2O_2 activation.

Heterogeneous catalyst		Fe^{2+} as homogeneous catalyst (ppm)	Reaction conditions				Pollutant			Ref.
Type	Dosage (g/L)		H_2O_2 (mmol/L)	pH	Light irradiation	Time (min)	Substrate	Content (ppm)	Removal	
WS_2	4	7.8	0.4	6.8	>420 nm	30	Phenol*	10	15%	[9]
MoS_2	0.30	4.0	0.1	5	>420 nm	30	Rhodamine B	20	30%	[10]
$MoS_{2-x}O_x$-220	0.20	2.0	0.6	4.0	None	30	Sulfamethoxazole	10	80%	[11]
Mo_2C	0.05	1.5	0.4	4.0	None	10	Rhodamine B	20	56.5%	[12]
Mo powder	0.05	224	0.5	5.8	None	5	Lissamine rhodamine B	20	20%	[13]
$Zn_xCd_{1-x}S$	0.10	112	0.8	5.5	>420 nm	25	Lissamine rhodamine B	30	65%	[14]
3D N-doped graphene aerogel sponge-loaded CoS_2	0.05	2.2	0.5	7.2	None	16	Ciprofloxacin	15	50%	[15]
$Mn\text{-}C_3N_4$	**0.10**	**0.26**	**1.0**	**7.0**	**>420 nm**	**60**	**Enrofloxacin**	**10**	**99%**	**This work**

* Contains 40 mg/L Cr(VI)

Reference

1 F. Liu, Z. Li, Q. Dong, C. Nie, S. Wang, B. Zhang, P. Han, M. Tong, *Environ. Sci. Technol.* 2022, **56**, 4413.

2 H. Xu, Q. Ye, J. Zhang, Q. Li, M. Wang, P. Zhou, G. Zhou, Q. Wang, *Sci. Total Environ.* 2021, **778**, 146280.

3 Q. Zhang, Y. Jin, L. Ma, Y. Zhang, C. Meng, C. Duan, *Angew. Chem. Int. Ed.* 2022, **61**, e202204918.

4 J. Luo, X. Wei, Y. Qiao, C. Wu, L. Li, L. Chen, J. Shi, *Adv. Mater.* 2023, **35**, 2210110.

5 X.-J. Wen, C.-G. Niu, L. Zhang, C. Liang, G.-M. Zeng, *Appl. Catal. B* 2018, **221**, 701.

6 C. Wang, L. Yin, Z. Xu, J. Niu, L.-A. Hou, *Chem. Eng. J.* 2017, **326**, 911.

7 R. Du, P. Chen, Q. Zhang, G. Yu, *Chemosphere* 2021, **273**, 128435.

8 K. Saravanakumar, C. M. Park, *Chem. Eng. J.* 2021, **423**, 130076.

9 C. Dong, J. Ji, B. Shen, M. Xing, J. Zhang, *Environ. Sci. Technol.* 2018, **52**, 11297.

10 M. Xing, W. Xu, C. Dong, Y. Bai, J. Zeng, Y. Zhou, J. Zhang, Y. Yin, *Chem* 2018, **4**, 1359.

11 X. Tan, W. Ding, Z. Jiang, L. Sun, Y. Huang, *Nano Res.* 2022, **15**, 1973.

12 F. Cheng, P. Zhou, Y. Liu, X. Huo, J. Zhang, Y. Yuan, H. Zhang, B. Lai, Y. Zhang, *Sci. Total Environ.* 2021, **797**, 149097.

13 Q. Yi, J. Ji, B. Shen, C. Dong, J. Liu, J. Zhang, M. Xing, *Environ. Sci. Technol.* 2019, **53**, 9725.

14 H. Yan, Y. Pan, X. Liao, Y. Zhu, C. Yin, R. Huang, C. Pan, *Appl. Surf. Sci.* 2022, **576**, 151881.

15 Y. Shi, Y. Hu, Y. Wang, X. Li, C. Xiao, J. Liu, Y. Chen, J. Cheng, X. Zhu, G. Wang, J. Xie, *J. Cleaner Prod.* 2022, **380**, 135008.